

## WIND TUNNEL MEASUREMENTS OF A CUBOID EXTERNAL LOAD MODEL

Niko Bier,  
Deutsches Zentrum für Luft- & Raumfahrt (DLR),  
Institute of Aerodynamics & Flow Technology,  
Lilienthalplatz 7, D-38108 Braunschweig, Germany

### Abstract

The prediction of the aerodynamic behavior of cuboid cargos in the vicinity of a releasing transport aircraft or as a slung load under a transporting helicopter is a challenging task, but can help to reduce the number of costly and time-consuming flight tests and wind tunnel campaigns. Against this background the DLR F20 model was built as a generic load configuration. It resembles a 108" x 88" cargo pallet in a scale of 1:2 and is equipped with 155 static and 5 unsteady pressure taps. Extensive measurements in the DNW-NWB low speed wind tunnel in Braunschweig were conducted as a first step to build a database for the aerodynamic coefficients of such cargo configurations and as a means to validate numerical simulations. Mean integral forces and moments were measured and a subsequent analysis of the data in the frequency domain showed no aerodynamically introduced frequencies. Surface pressure measurements were investigated and the traces of conical vortex structures were visible. Numerical in-tunnel simulations in the form of a feasibility study showed a good agreement with experimental values for configurations with small front surface and can serve as a means to apply suitable wind tunnel corrections.

### 1. INTRODUCTION

Being able to accurately and efficiently predict the behavior of loads and/or released stores in the vicinity of the carrying vehicle may help to ensure the safety of both, the carrier and the load [1] and can help to reduce the number of costly and time-consuming flight tests and wind tunnel campaigns [2] needed for certification.



**Fig. 1: The DLR F20 model in the DNW-NWB**

This holds especially for slung loads carried by a helicopter, e.g. cargo containers, where the load and center of gravity (CG) location may vary significantly and clearance of a new slung load is a long, expensive, and sometimes risky procedure of flight tests [3]. With a simulation tool comparable to the

one presented in [4], which allows real-time “what-if” analyses the implications of changes in weight, location of CG, etc. could be estimated in advance.



**Fig. 2: The DLR F20 model in configuration B**

However, it is evident that the quality of such a tool strongly depends on the dataset describing the aerodynamic properties of the load. Building such a dataset may become a challenging task, especially for bluff-body-configurations where the aerodynamic behavior is characterized by large separations, possibly re-attaching flow as well as unsteady phenomena like e.g. vortex shedding. Also changes in Reynolds number and the aspect ratio of front face to length as well as edge radii influence the aerodynamic behavior, e.g. the aerodynamic coefficients and the Strouhal number [5]-[7].

In order to generate such a dataset, it was therefore decided not to primarily make use of existing measurements and simulations of bluff body configurations, but to design the DLR F20 model as a generic load configuration and, thus come as close as possible to relevant reference aspect ratios, Reynolds- and Strouhal numbers.

## 2. GLOBAL MODEL DESIGN

The DLR F20 model, depicted in Fig. 1 and Fig. 2, resembles a 108" x 88" cargo pallet. In the design phase, the integration of the different model support systems available at the DNW NWB low speed wind tunnel in Braunschweig, Germany [8] was subject of careful consideration:

For symmetric onflow conditions it is desirable that no moments w.r.t. the model center and only a pure drag-force should be measured. However, this can only be achieved if also the model support system is designed symmetrically w.r.t. the incoming flow, e.g. by using a rear sting or a combined system of a ventral and a dorsal sting.

In the DNW-NWB a ventral, a dorsal and a rear sting are available for model mounting. But since the ventral and the dorsal mounting system cannot be applied simultaneously, a symmetric system could only be simulated by integrating a dummy-sting to the cargo model. The forces acting at the dummy sting then would have been difficult to handle.

On the other hand, the available rear sting might lead to aerodynamic effects similar to those of a splitter plate [9] and might change the aerodynamic behavior, i.e. the Strouhal number. In addition, it clearly affects the flow at the rear end of the model and probably the measured drag component.

In many cases the aerodynamic behavior of dropped cargos is primarily relevant in the near field of the releasing carrier, prior to the inflation of the main parachute system, esp. in the initial phase when aerodynamic angles are small. Here, often drag and pitching moment are the parameters of interest.

For slung loads under a helicopter side forces and moments assumable play a larger role than drag, and aerodynamic angles are also comparatively small at low speeds and in hover flights.

Because of these considerations, it was decided to measure the F20 model with a rear sting in order to minimize the influence of the mounting system on side forces and moments. However, the possibility to mount the model on a ventral sting in configuration *Config. A* (see below) to verify influences of the rear sting mounting on the Strouhal number was also part of the model specification.

With respect to the drag measurements, it was decided to choose the model scale  $S$  as large as possible. Thus, the missing integration area on the rear face of the model due to the rear sting would become relatively smaller and drag measurement, therefore, better. In addition, deviations in Reynolds and Strouhal number would become as small as possible.

On the other hand, a larger model scale results in a higher blockage and for large angles of attack or sideslip possibly in unrepresentative flow patterns due to significant wall interference effects.

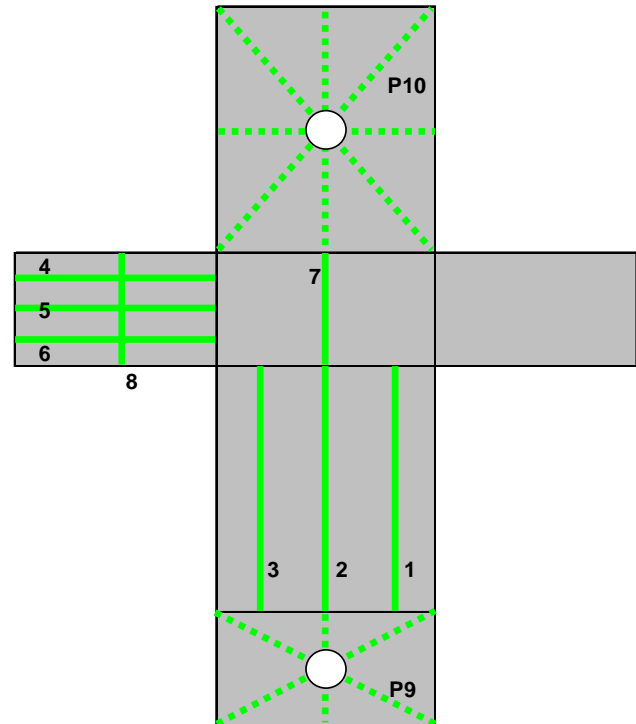


**Fig. 3: Arrangement of Pressure Tap Sections**

As a compromise, a scale of  $S = 1:2$  was chosen leading to a blockage of less than 10% at the most, depending on the actual angle of attack. Thus, the DLR F20 model features outer dimensions of 450 x 800 x 1000 mm. The model can be mounted onto the rear sting either with the smallest surface (*Config. A*, Fig. 1) or with the largest one facing upstream (*Config. B*, Fig. 2).

This allows the measurements to be interpreted as angle of attack sweeps larger than  $90^\circ$ , or to assess the influence of a variation the ratio of front face to length on the aerodynamic coefficients.

## 3. INSTRUMENTATION

On five of its faces the model is equipped with 155 pressure taps, distributed in eight pressure sections DV01 to DV08 and two patterns P9 and P10 on the rear panels of the two configurations *Config. A* and

*Config. B*. Fig. 3 shows the distributions in principle. The areas where the rear sting can become attached are highlighted as white circles. However, pressure taps are also incorporated into the corresponding closures.

Pressure sections 1 and 3 are placed at “spanwise” coordinates of  $\eta = \pm 0.75$ , sections 4 and 6 at a height of  $\zeta = \pm 0.67$ , both w.r.t the centre of the model. The remaining sections 2, 5 and 7 are placed in the middle of the corresponding surfaces.

With respect to *Config. A*, the taps in sections 1 to 6 feature a constant spacing of 50 mm in streamwise direction from the front to the middle and a constant spacing from 100 mm from the middle to the rear. The taps of the two patterns P9 and P10 were placed based on preceding numerical simulations in order to capture the pressure gradients across these surfaces. The patterns are arranged symmetrically w.r.t. the middle of the surfaces.

Five pressure taps, one in sections 2, 3 and 5 each and two in pattern P10, have been replaced by unsteady pressure sensors (“Kulites”) in order to produce validation data for later time-accurate numerical simulations.

#### 4. FLOW MEASUREMENTS

The model was tested in both configurations *Config. A* and *Config. B* in the closed test section of the DNW-NWB. But since the achievable positive and negative angles of attack are geometrically limited, a third configuration *Config. A'* was tested: *Config. A'* results from *Config. A* by rotating the model and the rear sting itself 180° around the sting-axis and is, thus, geometrically identical. However, since the pressure tap patterns on the top side and the bottom side are flipped, surface pressure distributions from *Config. A'* at a geometric angle of attack  $\alpha_{\text{geo}}$  can be seen as those from *Config. A* at an aerodynamic angle of attack  $\alpha = -\alpha_{\text{geo}}$ .

V = 30m/s		Alpha [°]															
		-4	-2	0	2	4	6	8	10	15	20	25	30	35	40	45	50
Beta [°]	-15																
	-8																
	0																
	2																
	4																
	6																
	8																
	10																
15																	

Fig. 4: Exemplary excerpt of the test matrix

The test matrix comprised variations of angles of attack and sideslip, also in combination, as well as different flow velocities. Fig. 4 exemplarily shows for a freestream velocity of  $v = 30$  m/s in green the

measured combinations of angle of attack and angle of sideslip.

During the wind tunnel campaign it turned out, that especially for onflow conditions with  $\alpha$  and  $\beta$  close to zero unexpected strong oscillations occurred. They could not only be stated in the measured forces, but caused the whole mounting, including the rear sting and the sword, to oscillate observably. However, the oscillations became smaller with increased angles of attack or sideslip.

For this reason only limited variations of the free stream velocity up to 45 m/s were possible. In addition, *Config. B* could even for small velocities only be measured for angles of attack larger than 10 degrees. The highest velocity of 45 m/s could only be measured for angles of attack larger than 30 degrees. Because of the strong oscillations the measurement integration time for averaging the global forces and moments was set to 11 seconds and later increased up to 29 seconds. However, distinct reference conditions were measured with integration times up to 71 seconds. The sampling rate of the data acquisition system was set to 1.2 kHz.

Since wind tunnel wall and support interference effects are difficult to correct, esp. for onflow conditions with larger angles of attack or sideslip, only the uncorrected wind tunnel data were analysed in a first step. In a second step numerical “in-tunnel” CFD simulations [10] with the DLR TAU-Code [11] are planned in terms of a feasibility study, hopefully allowing a better understanding of the effects of the mounting and the wind tunnel walls and to support the application of suitable wind tunnel corrections.

#### 5. EXPERIMENTAL RESULTS

Since *Config. B* at zero angle of attack could also be interpreted as *Config. A* under an angle of attack of 90°, the graphs presented hereafter show the measured data over a consolidated angle of attack  $\alpha^*$ , defined as follows:

$$(1) \quad \alpha^* = \begin{cases} \alpha & \text{for } \textit{Config. A and A'} \\ 90^\circ - \alpha & \text{for } \textit{Config. B} \end{cases}$$

The data are shown as dimensionless coefficients  $C$ , based on the uncorrected measured values  $V$  and, at any time, on the actual stagnation pressure and the actual front face, i.e. the projection of the model into a plane perpendicular to the incoming flow<sup>1</sup>:

<sup>1</sup> Angles of sideslip were not taken into account for the non-dimensionalization.

$$(2) \quad C = \frac{2 \cdot V}{\rho \cdot u_{\infty}^2 \cdot [0.8 \cdot \sin \alpha^* + 0.36 \cdot \cos \alpha^*]}$$

The coefficients are calculated in the aerodynamic coordinate system, if not stated otherwise.

### 5.1. Scatter of integral data

In a first step it was analyzed if the large oscillations in the support system can be linked to aerodynamic effects. Therefore the integral forces and moments were transformed into the frequency domain.

Fig. 5 exemplarily shows the force-component in X-direction in the body-fixed coordinate system for *Config. A* at an angle of attack of 10°, an angle of sideslip of 4° and an onflow velocity of 30 m/s.

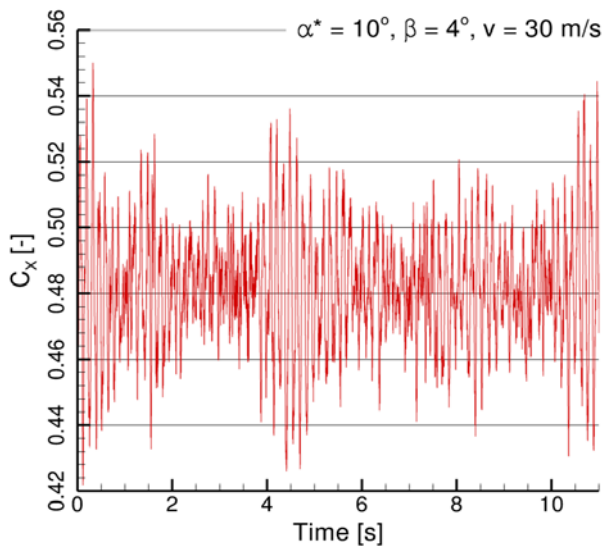


Fig. 5: Example of integral force in X-direction

Based on the assumption of a Gaussian distribution of the measured values the standard deviation of the force component in X-direction, i.e. direction of drag, lies within an order of magnitude of 0.02 or 4%, respectively. For the Z-direction, i.e. direction of lift, the standard deviation lies within an order of magnitude of 0.06 or 25%, respectively. For the side force the standard deviation lies within an order of magnitude of 0.05 or 55%, respectively.

For all three moments the standard deviation of the coefficients lies within an order of magnitude of 0.05. The corresponding relative values range from 65% for  $C_{MY}$  up to 200% for  $C_{MX}$ , respectively.

In a first approximation, the measured forces and moments as well as the corresponding standard deviations were found to be independent of the onflow velocity. In addition, no clear correlation between the angle of attack and the standard deviations of both, forces and moments, could be found. This holds for absolute values as well as for relative ones.

For a more pronounced orientation of the model at an increased angle of sideslip, however, the standard deviation of the side force component  $C_Y$  and the yawing moment  $C_{MZ}$  are increased together with the mean value, while  $C_{MX}$ - and  $C_{MY}$ -values (rolling and yawing moment) are decreased in terms of absolute and relative values. Fig. 6 summarizes the findings for selected onflow conditions.

$\beta$ [°]	15	4		4		4	
$\alpha$ [°]	10	10		32		48	
$v$ [m/s]	30	30	45	30	45	30	45
$\sigma$ (CX [-])	0,021	0,018	0,017	0,013	0,015	0,019	0,025
	4%	4%	4%	3%	3%	5%	7%
$\sigma$ (CY [-])	0,082	0,047	0,023	0,031	0,050	0,053	0,063
	36%	58%	28%	19%	30%	189%	468%
$\sigma$ (CZ [-])	0,070	0,060	0,071	0,037	0,052	0,090	0,094
	20%	23%	27%	4%	6%	7%	7%
$\sigma$ (CMX [-])	0,046	0,057	0,050	0,046	0,069	0,043	0,043
	95%	206%	183%	405%	598%	144%	106%
$\sigma$ (CMY [-])	0,037	0,053	0,069	0,023	0,033	0,038	0,034
	91%	66%	86%	65%	95%	60%	54%
$\sigma$ (CMZ [-])	0,050	0,042	0,038	0,029	0,026	0,035	0,034
	62%	97%	85%	168%	157%	186%	1079%

Fig. 6: Examples of standard deviations

### 5.2. Frequency domain

The transformation of the force components in X-direction into the frequency domain is exemplarily shown in Fig. 7 for three single runs. There are only minor differences to be seen:

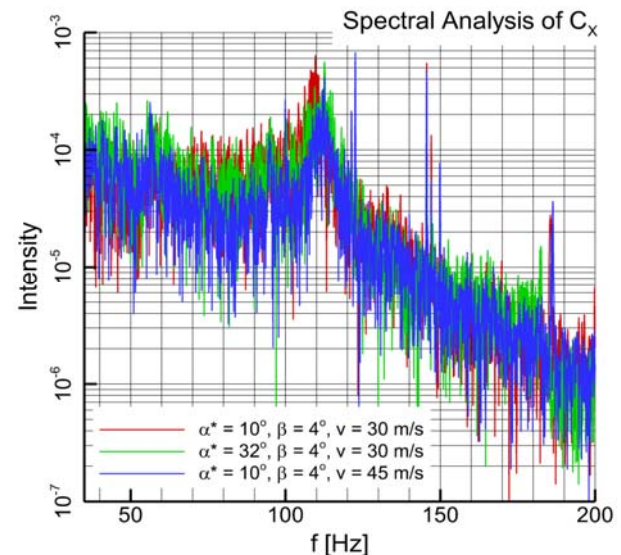


Fig. 7: Example of integral force in X-direction

The pronounced frequencies at 57 Hz, 110/112 Hz, 123 Hz, 146 - 150 Hz and 182/185 Hz are contained in all three test conditions. Especially at 122 Hz and 146 Hz the differences are almost only in the

intensity of the signal, so the peaks in the spectra are on top of each other within line-width.

Moreover, no frequency shift due to variations of the onflow velocity is observed (red vs. blue). This holds also for the other force-components and moments, for lower frequencies up to 1 Hz and for variations of angles of attack and/or angles of sideslip.

We conclude therefore that the large oscillations in the data are caused by an excitation of the model mounting system's eigenfrequencies.

Aerodynamic frequencies due to the highly detached flow seem to be either very low, i.e. less than 1 Hz, or higher than 200 Hz. Both cases were of little importance w.r.t. the scope of the experiments and were not investigated.

### 5.3. Integral forces and moments

Fig. 8 exemplarily shows for conditions without angle of sideslip the coefficients of lift (blue lines), drag (red lines) and pitching moment (green lines).

First of all, as expected, one can see only minor differences between *Config. A* and *Config. A'* (solid lines), indicating a good short-term repeatability of the experiments and a sufficient accuracy of the model mounting.

One can also see in the regime from  $45^\circ < \alpha^* < 50^\circ$  that the measurements of *Config. A* and *Config. B* match well, indicating only minor influences of the wind tunnel walls and the mounting.

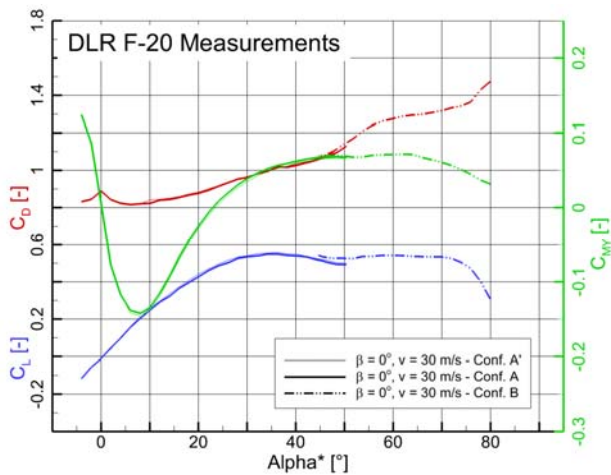


Fig. 8: Lift, drag and pitching moment for conditions w/o angle of sideslip

For the lift coefficient one can observe a linear correlation with the angle of attack in a regime close to the symmetric set-ups at  $\alpha^* = 0^\circ$  and  $\alpha^* = 90^\circ$ . For angles of attack in between, here:  $30^\circ < \alpha^* < 70^\circ$ , the lift coefficient is almost constant. The same can be stated for the pitching moment.

For the drag a continuous increase is observed,

because the ratio of front face to length influences the possibility of reattachments, the extension of the separation at the rear end, and thus the overall drag value. Unfortunately, as pointed out in section 4, no measurements were possible for  $\alpha^* = 90^\circ$ , but one can reasonably assume that lift and pitching moments would again become zero, as expected.

For the drag, a maximum value should be reached, possibly in the order of magnitude of  $C_D = 1.6 \dots 1.8$ , but extrapolations are very difficult since a local peak in the curve, as at  $\alpha^* = 0^\circ$ , is possible.

One can further notice that the gradients  $\partial C_L / \partial \alpha^*$  and  $\partial C_{MY} / \partial \alpha^*$  are dependent on the aspect ratio of front face to length, even if the absolute values are not affected.

Fig. 9 shows the effect of two angles of sideslip on the coefficients of lift (blue lines), drag (red lines) and pitching moment (green lines). For comparison the results for  $\beta = 0^\circ$  are incorporated as well.

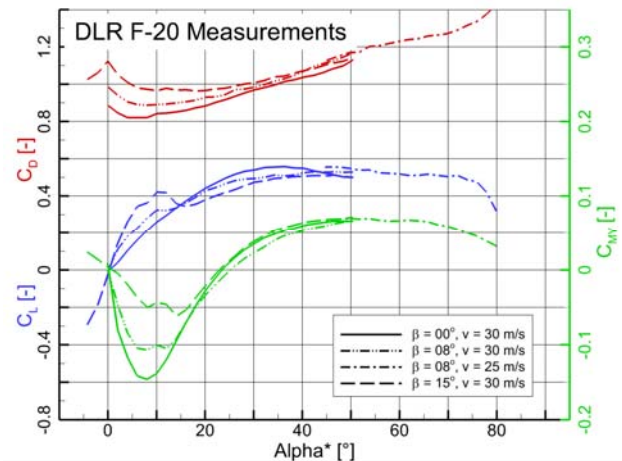


Fig. 9: Influence of angle of sideslip on lift, drag and pitching moment

For the lift coefficient close to  $\alpha^* = 0^\circ$  one can see an increased gradient  $\partial C_L / \partial \alpha^*$  with increased angle of sideslip. Between angles of attack  $5^\circ$  and  $15^\circ$  the lift-curve looks S-shaped and between  $20^\circ$  and  $45^\circ$  a slightly smaller lift coefficient is observed with increased angle of sideslip.

For the drag coefficient a slight increase with increasing angle of attack is observed. The effect becomes more pronounced near  $\alpha^* = 0^\circ$ .

For the pitching moment major effects can be seen in the range between  $0^\circ < \alpha^* < 20^\circ$  where the coefficient becomes less negative with increasing angle of sideslip, i.e. the configuration behaves more unstable.

The coefficients of the yawing moment (red) and the side force (blue) are shown for three selected conditions with angle of sideslip in Fig. 10.

The side force coefficients for  $\alpha^* \approx 0^\circ$  are nearly independent of the angle of sideslip. But since a yawing motion of a rectangular cylinder at a constant pitch angle of  $0^\circ$  is equivalent to a pitching motion at a yaw angle of  $0^\circ$ , some gradient would be expected between the single curves. We assume that the data is influenced by the asymmetric mounting – in this line of argument – and the side force data should be treated with special care.

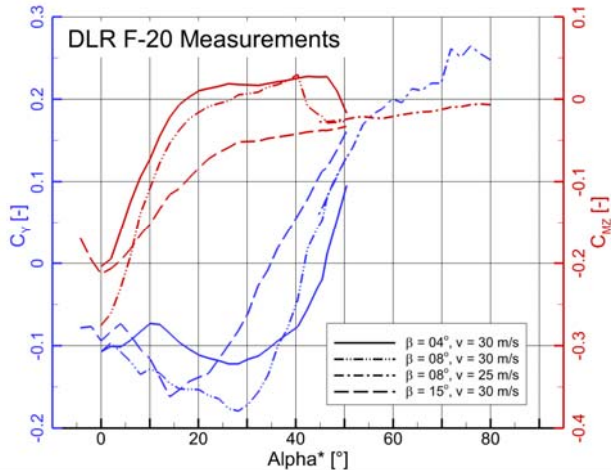


Fig. 10: Influence of angle of sideslip on side force and yawing moment

Interestingly, the yawing moment coefficient (red) at  $\alpha^* \approx 0^\circ$  behaves as one would expect, looking at the pitching moment of the configuration without angle of sideslip (Fig. 9): the back-turning moment has a maximum (negative values) at an angle of sideslip of  $8^\circ$  and becomes smaller afterwards.

Notable, the yawing moment stays negative for the whole range of angles of attack for the configuration with  $\beta \approx 15^\circ$ , other than the configurations in Fig. 9. The two other configurations reach small positive values, but between  $40^\circ < \alpha^* < 50^\circ$  the coefficient rapidly drops again to negative values.

At this point it is not clear whether this behavior is due to influences of the mounting, or probably a function of the aspect ratio.

Concluding w.r.t setting up a database for flight-mechanics simulations, we propose to carefully evaluate and process the measured data. This holds especially when distinct orientations, such as  $(\alpha, \beta) \gg 0^\circ$ , play a role or differing aspect ratios are of interest.

#### 5.4. Pressure distributions

To have the means at hand to validate numerical simulations of bluff body configurations, the DLR F20 model was equipped with pressure taps, as described in section 3 of this paper.

In a first step the pressure measurements were used as a more sensitive parameter than integral forces and moments, to check whether for symmetric onflow conditions symmetric flow patterns appear. Fig. 11 shows for *Config. A* at  $\beta = 0^\circ$  the pressure distributions in sections DV01 (blue) and DV03 (red) left and right of the center line of the model for four angles of attack, ranging from  $\alpha^* = 2^\circ \dots 38^\circ$ . The data is plotted against the length  $X$  of the model, starting from  $X = -500$  mm at the front end to  $X = 500$  mm at the rear end. For better readability, each pair of curves at one specific  $\alpha^*$  has been shifted individually, since only the pressure difference is of importance.

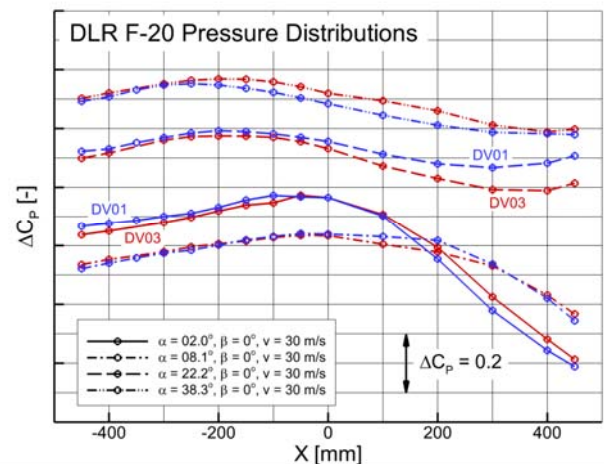


Fig. 11: Examples of surface pressure distributions in sections DV01 and DV03

One can see that for all angles of attack only minor differences in absolute values can be seen, while especially the position of minima and maxima matches. This holds also for higher angles of attack up to  $\alpha^* = 50^\circ$  (not shown). Also there is no evidence that any tap in these two cuts gives disturbed values due to imperfections in manufacturing, handling, etc.

However, for some angles of attack the pressure distributions in the aft region of the model between  $100 < X < 500$  don't match perfectly (e.g. Fig. 11,  $\alpha^* = 22.2^\circ$ ). We attribute this to the highly unsteady separated flow. In addition the integration time was probably not chosen long enough, since for other angles of attack (not shown) the curves match again or the then upper curve becomes the lower one.

The pressure distributions for *Config. A* at  $\beta = 0^\circ$  in DV02 (solid lines) in the symmetry plane and DV03 (dash-dotted lines) are shown for three angles of attack in Fig. 12. The selected angles of attack cover the  $\alpha^*$ -range of minimum  $C_{MY}$ -values (see Fig. 8) and show symmetric pressure distributions in DV01 and DV03.

For an angle of attack of  $0^\circ$  (blue lines) the flow pattern w.r.t. the symmetry plane is symmetric for a wide spanwise and chordwise extension, except for the front corners, where lower pressure levels can be seen. Since the pressure level is almost always below  $C_p \approx -0.2$ , we assume that there is probably no stagnation line, i.e. no re-attachment, on the top surface. The main flow direction inside the large separation bubble starting at the front edge at the latest, would then be orientated upstream, i.e. in the direction of negative X-values.

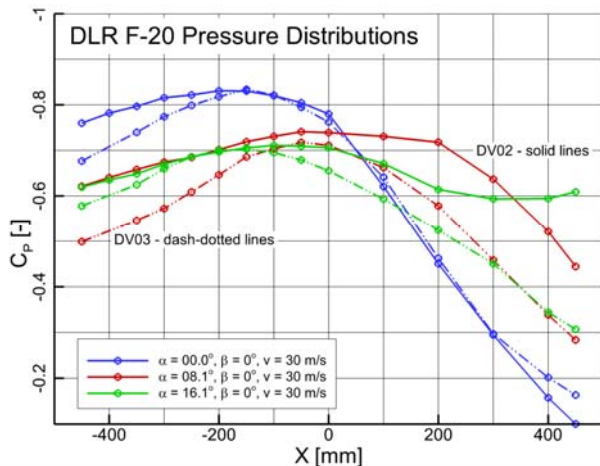


Fig. 12: Examples of surface pressure distributions in sections DV02 and DV03

For an increased angle of attack of  $8.1^\circ$  (red lines) the flow pattern seems still to be symmetrical in spanwise direction. From the lower pressure level near the rear end of the model, we conclude the separation bubble over the top surface became larger than for  $\alpha^* = 0^\circ$ , as one would expect.

For an angle of attack of  $16.1^\circ$  the flow pattern at the rear end of the model starts to differ in spanwise extension and pressure values become even lower because of the further increased size of the separation bubble. However, since in DV02 a plateau with almost constant  $C_p$ -values between  $250 < X < 400$  mm can be seen, probably because of an interaction with the expected conical vortex structures emerging from the front edges [7]

Fig. 13 shows the pressure distributions on the side for the pressure sections DV04 (solid lines) near the bottom and DV06 (dash-dotted lines) near the top of the F20 model.

For an angle of attack of  $0^\circ$  (blue lines) one can see a symmetric pressure distribution which on the one side was desirable, but on the other not necessarily expected because the complete model mounting system is not symmetric in Z-direction. However, this influence can obviously be neglected.

When the angle of attack gets increased to  $\alpha^* = 8.1^\circ$

(red lines) one can see that the area of pressure rise starts earlier in DV04 near the bottom than in DV06 near the top of the model. Also the pressure level is lower near the bottom than at the top. We therefore conclude that the minimum pressure level correlates with the trace of the conical vortex structure emerging at the lower front edge. This assumption is supported by the pressure distributions at an angle of attack of  $16.1^\circ$  (green lines) where the minima are stronger and have moved upstream in comparison to  $\alpha^* = 8.1^\circ$ .

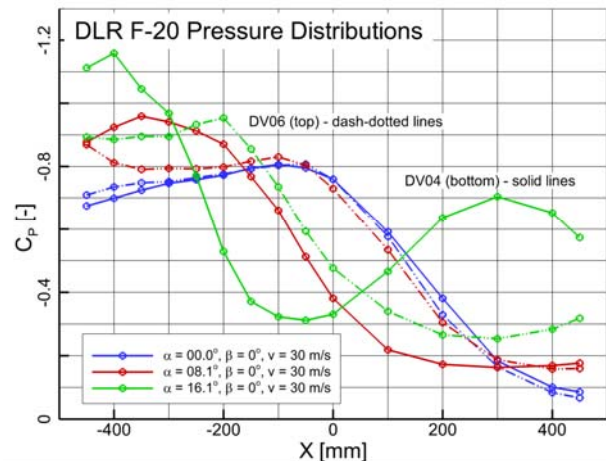


Fig. 13: Examples of surface pressure distributions in sections DV04 and DV06

For the angle of attack of  $16.1^\circ$  a second minimum in the pressure level can be seen in DV04 near the rear end of the model. We contribute this to the formation of new vortex structures emerging from the edges on the lower side near the rear end of the model.

The pressure distribution on the bottom side of the model is shown color-coded in Fig. 14. The values inside the large circles belong to an angle of attack of  $8.1^\circ$ . The medium sized circles show the values at an angle of attack of  $20.1^\circ$  and the color inside the small circles show the pressure at an angle of attack of  $46.4^\circ$ .

The relatively large negative pressure coefficients in the outside front region (large circles, red color) for the two smaller angles of attack are also very likely linked to the formation of the aforementioned vortex structures. With increasing angle of attack, these areas move upstream (medium sized circles, green color at  $X = -300$  mm), as one would expect.

The highest angle of attack depicted (small circles, blue color,  $\alpha^* = 46.4^\circ$ ) shows a sudden change in the flow pattern when the main stagnation line jumps from the front surface to the lower surface.

However, the flow pattern on the rear part of the lower surface seems unaffected by this principal

change in flow topology. This is probably because the effective length of the model w.r.t. the main flow direction is significantly shorter than for lower angles of attack and the area of detached flow behind the model still dominates the separated flow here.

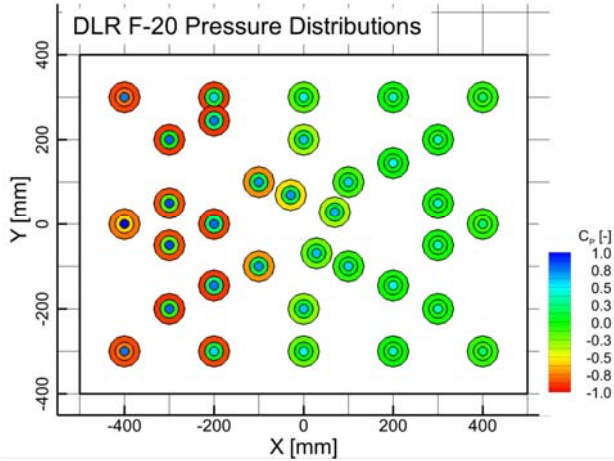


Fig. 14: Examples of surface pressure distributions on the bottom side (P10)

The pressure levels on the rear surface of the model are depicted in Fig. 15 in the same way than previously discussed in Fig. 14, except for a much narrower  $C_p$ -scale.

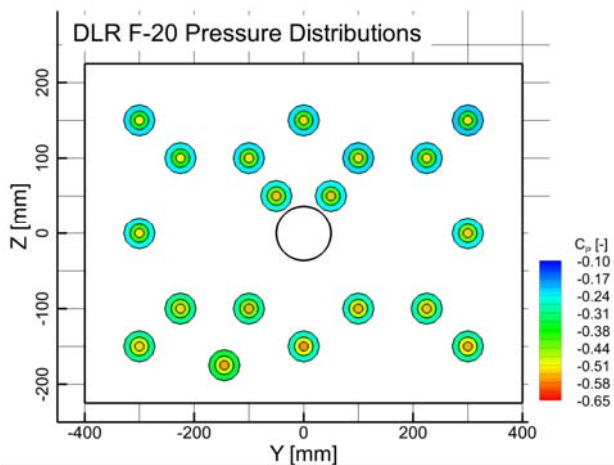


Fig. 15: Examples of surface pressure distributions on the rear side (P9)

For each angle of attack (circles of different sizes) a comparatively homogeneous pressure distribution with only minor gradients between top and bottom can be seen. However, for increased angles of attack (smaller circles) the mean pressure level drops. This is most likely an effect due to the increased ratio of effective front face vs. effective length of the model and the comparatively increased size of the area of detached flow behind the model and thus, the larger velocities near the surface.

For onflow conditions with an angle of sideslip of  $15^\circ$  as depicted in Fig. 16, the pressure distribution still shows no major gradients on the rear surface for a low angle of attack of  $8^\circ$  (large circles). However, with increasing angle of attack over  $20.1^\circ$  (medium circles) to  $46.4^\circ$  (small circles) pressure gradients become more pronounced, both from top to the bottom and in spanwise direction.

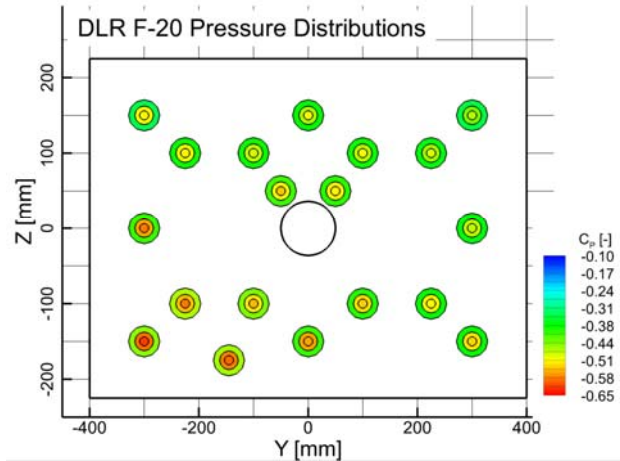


Fig. 16: Examples of surface pressure distributions on the rear side (P9) for  $\beta = 15^\circ$

For the challenging issue to correct the measured drag values, at least the missing integration surface due to the opening for the sting seems to be correctable: Since pressure gradients don't seem to play a major role on the rear surface in the vicinity of the penetration – the lower two taps at  $Z = -50$  and  $Y = \pm 50$  mm were unfortunately damaged during the mounting – the mean value of the static pressure is sufficiently accurate to account for the missing integration surface. However, whether or not the flow downstream the rear surface is globally affected by the mounting cannot be answered.

The pressure distribution in pattern P10 on the rear surface of *Config. B* is exemplarily depicted Fig. 17 for three measurement points at constant conditions  $\alpha^* = 40^\circ$ ,  $\beta = 0^\circ$  and an onflow velocity of 40 m/s. The results of the three runs are plotted at the position of the pressure taps in a color coded way in squares of different size. In addition the penetration for the rear string is indicated as a black circle.

Although the angle of sideslip is set to zero, no symmetric flow pattern on the left and on the right side appears. In fact, the color-distribution looks somewhat “random”. However, since the integration time of 71 seconds is assumable long enough to filter any frequency above 0.1 Hz and since the results of all three runs match, we think that the “real” mean values are captured.

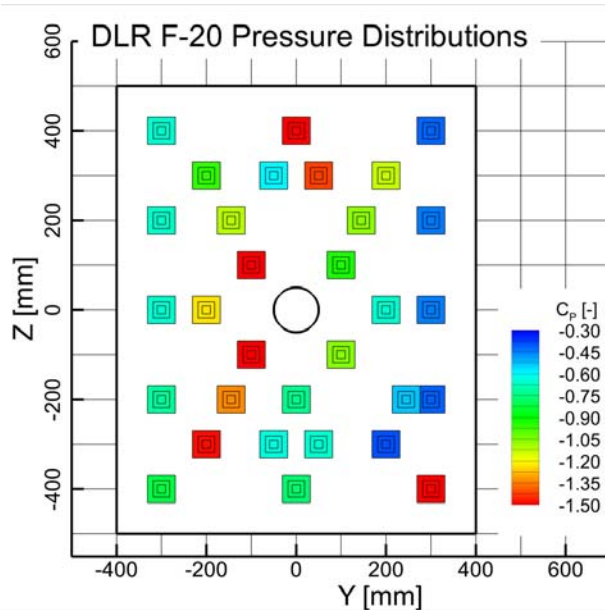


Fig. 17: Examples of surface pressure distributions on the rear side (P10)

With respect to the correction of the measured drag, a configuration with such a low aspect ratio seems to be a bit more difficult to handle since there is a notable pressure gradient in the vicinity of the penetration. In addition, whether or not the flow downstream the rear surface is globally affected by the mounting cannot be answered, either.

### 5.5. Unsteady pressure distributions

As described in section 3 of this paper, the DLR F20 model was also equipped with five unsteady pressure sensors (“Kulites”) complementary to the static pressure taps.

With respect to *Config. A*, two *Kulites* were placed near the front edge in sections DV02 and DV03 on the top surface and on the lower surface near the front edge, opposite to the one in DV03. The fourth *Kulite* was placed on the center line of the lower surface at 75% of the model length. The last one was placed near the center of DV05 on the side of the model.

With respect to *Config. B* the *Kulites* then come to lie on the front surface near the bottom (DV02 and DV03), on the rear surface near the bottom, opposite to the one in DV03, and on the center line of the rear surface, just above the penetration for the sting. The last one then lies again on the model's side surface near the center of DV05.

The pressure data were measured at a frequency of 1.2 kHz, using a low pass filter of 0.6 kHz. The integration time was increased up to 79 sec per measurement point and variations of the onflow velocity were performed to distinguish aerodynamic frequencies from the system's eigenfrequencies.

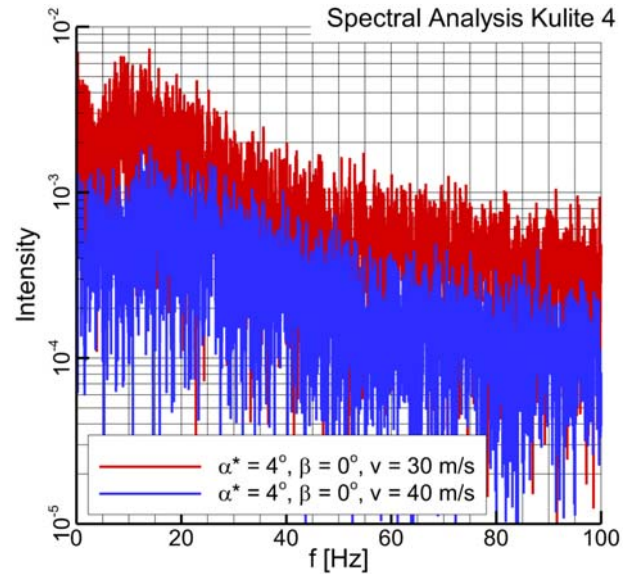


Fig. 18: Spectral analysis of Kulite 4

Fig. 18 exemplarily shows for *Config. A* the result of a preliminary transformation of the measured data into the frequency domain for Kulite 4 in DV03, i.e. at the front of the top surface, for two different onflow velocities. For better readability, the intensity for the higher velocity (blue line) was scaled with a factor of 0.3. For both cases there are no distinct frequencies to be seen, especially no shifts with a factor of 4:3. The same holds also for the other *Kulites*, also at other angles of attack and/or for *Config. B*. However, it is planned to deeper analyze the data since there seems to be too much noise in the data.

## 6. NUMERICAL SIMULATIONS

As discussed in the beginning, complementary numerical simulations with the DLR TAU-Code were conducted to better understand the complex flow topology and the influence of the wind tunnel walls and the model support on the measured data.

A comparison of numerical trajectory simulations of cuboid cargos released from a transport aircraft [12] with measurements in the DNW-NWB as well as comparisons of steady state Reynolds-averaged Navier-Stokes-simulations with different turbulence models [13] with experimental flow field data from PIV measurements in the DNW-NWB indicate, that a steady state RANS-approach with the turbulence model from Spallart-Allmaras (SA) [14] may well be appropriate within the scope of this investigation.

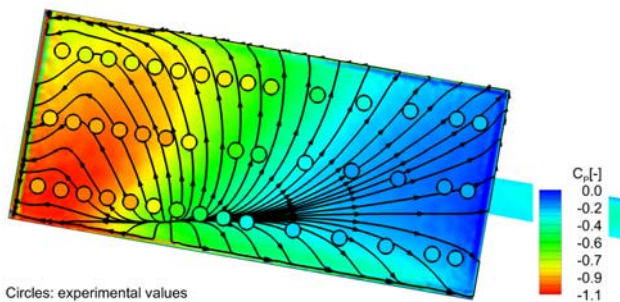
The numerical simulations comprised four set-ups:

- The first two simulations targeted *Config. A* and *Config. B* inside the wind tunnel, including the model mounting, at  $\alpha^* = 10^\circ$  and  $\beta = 0^\circ$ .

- The third simulation targeted *Config. A* inside the wind tunnel at  $\alpha^* = 10^\circ$  and  $\beta = 0^\circ$ , but without the model mounting, in order to assess the impact of the rear sting on the global flow pattern.
- The fourth simulation targeted *Config. A* in free-flight conditions at  $\alpha^* = 10^\circ$  and  $\beta = 0^\circ$ .

For the in-tunnel simulations only the first-order effects due to the wind tunnel walls were of interest. Consequently the test section was modelled by inviscid, non-divergent walls of a large extension of 500m up- and downstream of the test section.

A comparison of the numerical results and the experimental values is exemplarily shown in Fig. 19 for *Config. A*:



Circles: experimental values

Fig. 19: Exemplary comparison of experiments and in-tunnel simulation

The agreement between the experiment (values inside the circles) and the numerical approach is very good for this case. Only the location of the conical vortex structure emerging from the lower front corner (red-orange area) shows deviations and ends a bit too far upstream at the top of the model.

Further analysis (not shown) [15] revealed that, as a consequence, also the pressure signature at the top is influenced and the pressure rise towards the rear end starts too early in comparison with the experiments. On the bottom side the agreement is good again, which, as a result, leads to deviations in the predicted pitching-moment.

On the rear side the agreement is fair in terms of global flow features but reasonably good in terms of absolute numbers, although the SA turbulence model is not designed to predict the flow within large separated areas. As a consequence the agreement on most surfaces is poor for *Config. B*.

However, for *Config. A* at an angle of attack of  $10^\circ$ , where the agreement is good, the numerical simulations indicate, that there is a significant influence of the wind tunnel walls on the measured coefficients, especially on lift and drag.

## 7. CONCLUSION

Based on the DLR F20 model a comprehensive dataset of the force and moment coefficients of a cuboid external load model has been generated. The dataset comprises variations of angle of attack, angle of sideslip and the ratio of front face to length.

However, since the data are uncorrected w.r.t. wind tunnel walls and support interference effects, making use of the data, e.g. for building look-up tables for flight-mechanics-driven simulation environments, is not straightforward. This holds especially since numerical simulations indicate a significant influence of the wind tunnel walls.

However, making use of e.g. time-accurate large eddy (LES) or detached eddy simulations (DES) together with more sophisticated turbulence models, e.g. Reynolds-stress models (RSM) can help to correct the measurements. For validation purposes, time accurate force and moment data, as well as pressure data was recorded.

## 8. REFERENCES

- [1] Hooker J.R., Gudenkauf J.A.: *Application of the Unstructured Chimera Method for Rapid Weapons Trajectory Simulations*. 45th AIAA Aerospace Sciences Meeting, Reno (NV), Paper 2007-75, 2007.
- [2] Cenko, A.: *Lessons Learned in 30 years of Store Separation Testing*. 47th AIAA Aerospace Sciences Meeting, Orlando (FL), Paper 2009-98, 2009.
- [3] Raz R., Rosen A., Cicolani L. and Lusardi J.: *Using Wind Tunnel Tests for Slung-Load Clearance, Part 1: The CONEX Cargo Container*. Journal of the American Helicopter Society, Vol. 59, 2014.
- [4] Jann T., Geisbauer S., Bier N., Krüger W.-R., Schmidt H.: *Multi-Fidelity Simulation of Cargo Airdrop*. AIAA Aviation 2015, Paper 2015-2654, Dallas (TX), 2015.
- [5] Bruno, L., Salvetti, M.V., Ricciardelli, F.: *Benchmark on the Aerodynamics of a Rectangular 5:1 Cylinder*. Journal of Wind Engineering and Industrial Aerodynamics, Vol. 126, 2014, pp. 87–106.
- [6] Schewe, G.: *Reynolds number-effects in flow around a rectangular cylinder with aspect ratio 1:5*. Journal of Fluids and Structures, Vol. 39, 2013, pp.15–26.
- [7] Hucho, W.-H.: *Aerodynamik der stumpfen Körper*. 2. Auflage, 2012.
- [8] Bergmann, A.: *The Aeroacoustic Wind Tunnel DNW-NWB*. 18th AIAA/CEAS Aeroacoustics Conference, Colorado Springs (CO), Paper 2012-2713, 2013.
- [9] Bearman, P.W.: *Investigation of the flow behind a two-dimensional model with a blunt trailing edge fitted with splitter plates*. Journal of Fluid Mechanics, Vol. 21, 1965, pp. 241-255.

- [10] Melber-Wilkending, S., Wichmann, G.: *Application of Advanced CFD Tools for High Reynolds Number Testing*. 47th AIAA Aerospace Sciences Meeting, Paper 2009-0418, 2009.
- [11] Schwamborn, D. et al.: *The DLR TAU-Code: Recent Applications in Research and Industry*. In Wesseling, P., Onate, E., Perieaux, J. (Eds.): *Proceedings of the European Conference on Computational Fluid Dynamics*. ECCOMAS, 2006.
- [12] Schade, N.: *Simulation of Trajectories of Cuboid Cargos Released from a Generic Transport Aircraft*. 29th AIAA Applied Aerodynamics Conference, Paper 2011-3959, Honolulu (HI), 2011.
- [13] Geisbauer, S.; Bier, N. et al: *Validation of the Flow Topology Around Several Airdrop Cargo Configurations at Static Conditions*. 31st AIAA Applied Aerodynamics Conference, Paper 2013-3155, San Diego (CA), 2013.
- [14] Spalart, P., Allmaras, S.: *A One-Equation Turbulence Model for Aerodynamic Flows*. AIAA, Paper 1992-439, 1992.
- [15] Rabe, D.: *Simulation abgelöster Strömungen um stumpfe Körper mit scharfen Kanten*. Bachelor thesis, Braunschweig, 2014.